Biomaterials Science

ROYAL SOCIETY OF CHEMISTRY

PAPER

View Article Online
View Journal | View Issue

Cite this: *Biomater. Sci.*, 2023, **11**, 5618

An injectable supramolecular hydrogel as a self-drug-delivery system for local chemoimmunotherapy against melanoma†

Sourabh Bera, Hemanta Kumar Datta and Parthasarathi Dastidar *

Received 3rd May 2023,
Accepted 22nd June 2023

DOI: 10.1039/d3bm00758h

rsc.li/biomaterials-science

Skin-cancer melanoma caused 57k death in 2020. Some of the available therapies are: topical application of a gel loaded with an anti-skin cancer drug and intravenous injection of immune cytokines; however, both the approaches have drawbacks such as inefficient internalization of the drug in cancer cells and a short half-life with severe side effects, respectively. Interestingly, we observed for the first time that a subcutaneously implanted hydrogel designed and synthesized by coordinating NSAIDs and 5-AP with Zn(II) can effectively combat melanoma cell (B16-F10)-induced tumors in C57BL/6 mice. Both *in vitro* and *in vivo* results show that it can effectively reduce PGE_2 expression, consequently upregulating IFN-γ and IL-12 that eventually engage M1-macrophages for activating T cells ($CD8^+$), triggering apoptosis. This unique all-in-one self-drug-delivery approach, wherein the hydrogel implant is made from the drug molecules itself providing both chemotherapy and immunotherapy in combating deadly melanoma, highlights the supramolecular chemistry-based bottom-up approach in cancer therapy.

1 Introduction

Cancer is the second leading cause of death worldwide.[1] According to the report published by the World Health Organisation (WHO) in 2022, 57k people died worldwide in 2020 from melanoma only.[2] Most often, anticancer drugs are administered *via* the intravenous route, triggering unwanted toxicity in healthy tissues and causing severe side effects. To minimize this, intravenous nanomedicines targeting tumor sites are being developed.[3–5] However, local chemotherapy to the tumor site appears promising because of high local concentration, a longer retention time, and slow and sustained release of the drug to the tumor site which consequently increases the anticancer potential and minimizes the chance of affecting healthy tissues. Drug-encapsulated hydrogel formulations are promising because of the biocompatibility of the gelling solvent (water) and its easy administration to the tumor site *via* the topical or subcutaneous route.

To avoid synthetic vehicle-related toxicities, a hydrogel matrix can be obtained from natural polymers, synthetic peptides, proteins, nucleic acids, *etc*.[6–8] Boronic ester formation induced cross-linked polymer-based hydrogels to load and release erlotinib (anticancer drug)[9] and aPDL1 (antibody of programmed death ligand 1),[10,11] cross-linked nucleic acid nanogels for effective siRNA delivery,[12] sequestering ATP by a designed peptide-based hydrogel to boost the activity of the anticancer drug doxorubicin (DOX),[13] DNA gel nanoparticles for tumor therapy,[14] protocatechualdehyde-based Fe(III) metallo-hydrogels for loading and release of DOX,[15] gelatin-based hydrogels loaded with a NO donor for anti-tumor immunotherapy,[16] supramolecular hydrogels releasing both DOX and an immunosuppressive agent for cancer therapy,[17] and syringeable immunomodulatory multidomain nanogels for tumor immunotherapy[18] were reported to be effective, as evident from both *in vitro* and *in vivo* experiments.

Designing such formulations requires careful choice of a hydrogel matrix that should be sustainable, biocompatible, biodegradable, *etc*. However, gaining access to such a hydrogel matrix often requires a nontrivial synthetic protocol (for example, a peptide-based hydrogel matrix); it must also be amenable for facile loading of drugs and suitable for slow and sustained release of drugs, avoiding burst release.

School of Chemical Sciences, Indian Association for the Cultivation of Science (IACS), 2A and 2B, Raja S. C. Mullick Road, Jadavpur, Kolkata-700032, West Bengal, India. E-mail: ocpd@iacs.res.in, ocpdastidar@gmail.com

†Electronic supplementary information (ESI) available: Synthesis and characterization data of the CCs (FT-IR spectra, SXRD, crystallographic table, ORTEP plot, PXRD plot); gel characterization (amplitude sweep, TEM, FT-IR); *in vitro* experiments (MTT assay, drug internalization, membrane permeability, nuclear condensation, cell migration, ROS, Hoechst efflux assay and cell cycle); *in vivo* experiments (tumor volume, images of the tumor bearing mice, component-treated tumor images, size, weight, body weight, drug internalization, annexin V-FITC, MMP, histopathology, ROS and Hoechst efflux assay); PGE_2 assay; the *in vivo* immunomodulation study (PDF); Supplementary movies 1–5 (ZIP). CCDC 1918448–1918451 (**CC-1–CC-4**). For ESI and crystallographic data in CIF or other electronic format see DOI: **https://doi.org/10.1039/d3bm00758h**

An alternative approach [known as self-drug-delivery (SDD)], wherein a drug molecule is converted to a supramolecular gel,[19–34] is being investigated with much interest, because in here, one can avoid the challenges involved in the design and synthesis of a gel matrix and the drug can be delivered by itself to the target site;[35–38] for example, a hydrogel obtained by sonicating the anticancer drug raltitrexed was found to be effective in treating post-surgical cancer.[39] A plasma-activated thermosensitive biogel as an exogenous ROS carrier for post-surgical treatment of cancer was developed.[40] An injectable and biodegradable DNA hydrogel was reported to be effective in tumor therapy.[14] A trident peptide-based hydrogel functionalized with phosphotyrosine, camptothecin and hydroxychloroquine was demonstrated to be effective in enhanced chemotherapy and immunotherapy for spatial suppression of tumor metastasis.[41]

Most of these fascinating SDD systems, however, were dependent on one way or the other on covalent synthesis, which is relatively difficult compared to metal–ligand coordination chemistry. Drug delivery systems developed by exploiting metal–ligand coordination chemistry offer various advantages over covalent chemistry-based systems: they (a) are easily synthesized, (b) are amenable for atomic-level structure determination by single-crystal X-ray diffraction (SXRD), providing crucial insights for further development, (c) have tuneable physicochemical properties arising from virtually infinite combinations of ligands (drug molecules) and metal salts, and (d) are easily biodegradable owing to the relatively labile metal–ligand coordination bond compared to the covalent bond.[42–46]

We have developed a few metal–ligand coordination-based SDD systems that include non-steroidal anti-inflammatory drug (NSAID)-anchored Zn(II) coordination polymer-based metallogels effective in inhibiting cell migration of melanoma cells B16-F10[47,48] and multi-drug-derived Zn(II) coordination polymer-based nano-sized particles for killing both *Mycobacterium tuberculosis* and the human lung cancer cell line A549 with no *in vivo* toxicity.[49]

With this background in mind, we set out to develop an SDD system by exploiting simple coordination chemistry that would target melanoma skin cancer. Herein, we report the design, synthesis and single crystal structures of a series of Zn (II) coordination complexes (CCs) derived from 5-amino-1,10-phenanthroline (5-AP) and various NSAIDs (meclofenac – MEC, diclofenac – DIC, mefenamic acid – MEF and flufenamic acid – FLU). A majority of the CCs formed highly stable hydrogels at room temperature. MEC-derived CCs showed significant anticancer activity in both MTT and scratch assays against the melanoma cell line B16-F10. Further *in vitro* experiments (cell cycle, nuclear condensation, annexin V-FITC/PI, mitochondrial membrane potential (MMP), Hoechst efflux assays) suggested an apoptotic pathway. *In vivo* experiments by subcutaneous injection of an MEC-derived hydrogel (MHG-1) to the melanoma-induced tumor site in a C57BL/6 mouse model showed a remarkable anti-tumor effect; upregulation of pro-inflammatory cytokines (IFN-γ, TNF-α, IL-12, IL-2 and IL-6) observed in the hydrogel-treated tumor tissue further supported the apoptotic pathway and increased the cytotoxic T cell population, suggesting the role of the hydrogel in anti-tumor immunity (Scheme 1).

2 Results and discussion

2.1 Design, synthesis and single crystal structures of the CCs

The main objective of the present work was to develop a hydrogel-based SDD system that can subcutaneously be implanted on the tumor site for plausible anti-tumor therapy. For this purpose, we exploited simple coordination chemistry, wherein, we employed a N donor chelating ligand, namely 5-AP, various Na-NSAIDs (MEC, DIC, MEF and FLU), and $Zn(NO_3)_2$ to synthesize a series of Zn(II) CCs as potential anticancer agents against melanoma-induced tumors (Fig. 1A). While 5-AP metal complexes are reported to have anticancer properties,[50] NSAIDs are known for their immunomodulatory effects on tumor microenvironments;[51] Zn salts, on the other hand, do possess anti-inflammatory properties,[52] which is an advantage in the context of cancer therapy. It is well known that hydrogen bonding and hydrophobic/hydrophilic balance play a crucial role in the supramolecular hydrogelation process.[53,54] Thus, a large π surface of 5-AP and hydrogen bonding functionalities ($-NH_2$ of 5-AP and –COO and –NH of the NSAIDs) are expected to facilitate the hydrogelation process under suitable conditions.

2.1.1 Single crystal structures. Mixing 5-AP/Na-NSAID/$Zn(NO_3)_2$ at a 1 : 2 : 1 molar ratio in EtOH/MeOH/water (4 : 4 : 1 v/v/v) at room temperature, followed by slow evaporation in a long tube yielded crystalline products after one week (Fig. 1A). Blue shift ($\Delta\nu$ = 6–41 cm^{-1}) of the carboxylate stretching with respect to that of the corresponding Na-NSAID in the FT-IR of these crystals strongly suggested carboxylate-Zn coordination (Fig. S1 and Table S1†). Elemental analysis clearly supported the stoichiometry, suggesting the formation of Zn(5-AP)$(NSAID)_2$ complexes (see the Experimental section).

Single crystals of these complexes were subjected to X-ray diffraction (Table S2†). While **CC-1** and **CC-4** were isomorphous, displaying an identical space group (triclinic, $P\bar{1}$) and near identical cell dimensions, **CC-2** and **CC-3** belonged to a monoclinic crystal system with space groups $P2/c$ and Pc, respectively. Except in **CC-4**, the metal centre Zn(II) was six coordinated, owing to the chelating coordination mode of both 5-AP and carboxylates of the corresponding NSAID moieties; mono-dentate coordination of one of the NSAID moieties in **CC-4** resulted in five coordinated Zn(II) species, suggesting the formation of coordination complexes having a general formula Zn(5-AP)$(NSAID)_2$ (Fig. 1B). Interestingly, only **CC-3** contained a lattice occluded solvate molecule (EtOH) in its asymmetric unit. It may also be noted that half of the complex molecule was located in the asymmetric unit in **CC-2** as the metal centre Zn(II) resided on a 2-fold axis consequently inducing a rotational disorder on 5-AP. Careful analyses revealed that the N atom of the disordered 5-AP moiety was involved in hydro-

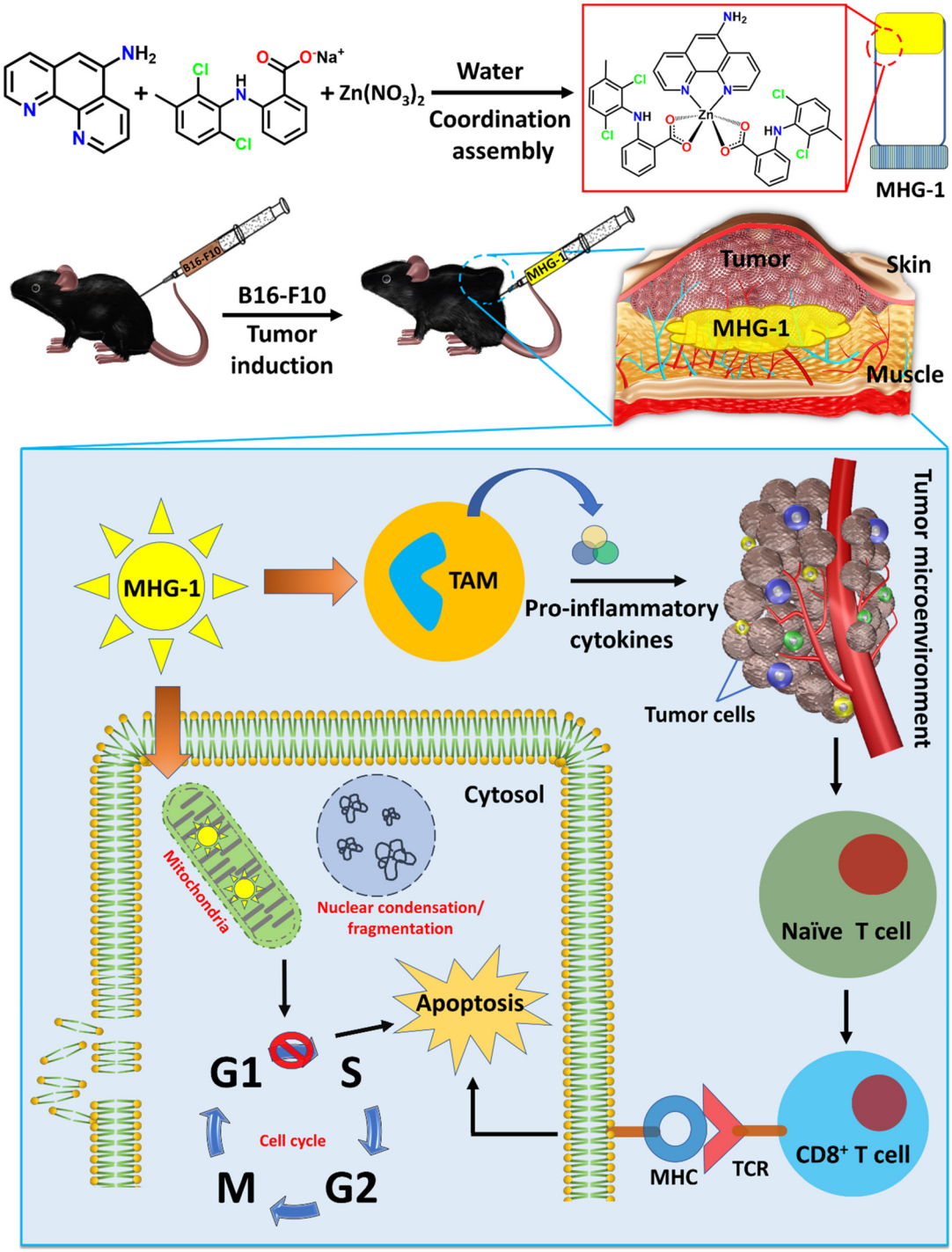

Scheme 1 Schematic representation of the work done here (TAM: tumor associated macrophages; MHG-1: metallohydrogel-1; MHC: major histocompatibility complex; TCR: T cell receptor).

gen bonding with the carboxylate O atoms of the neighbouring molecules (Fig. S3 and Table S4†). However, in the remaining cases, the complex molecules were located at general positions. Molecular self-assembly in all the crystal structures was mainly governed by hydrogen bonding and π–π stacking. Driven by strong intermolecular N–H···O hydrogen bonding involving the amino N and carboxylate O atoms and π–π stacking interactions involving the large π surface of 5-AP, both **CC-1** and **CC-4** formed centrosymmetric dimers, which were further packed in the crystal structures sustained by π–π stacking interactions involving 5-AP and F-containing phenyl moieties (Fig. S2 and S5 and Tables S3 and S6†). In **CC-3**, the coordination complex molecules formed a hydrogen bonded chain through N–H···O interactions involving the carboxylate

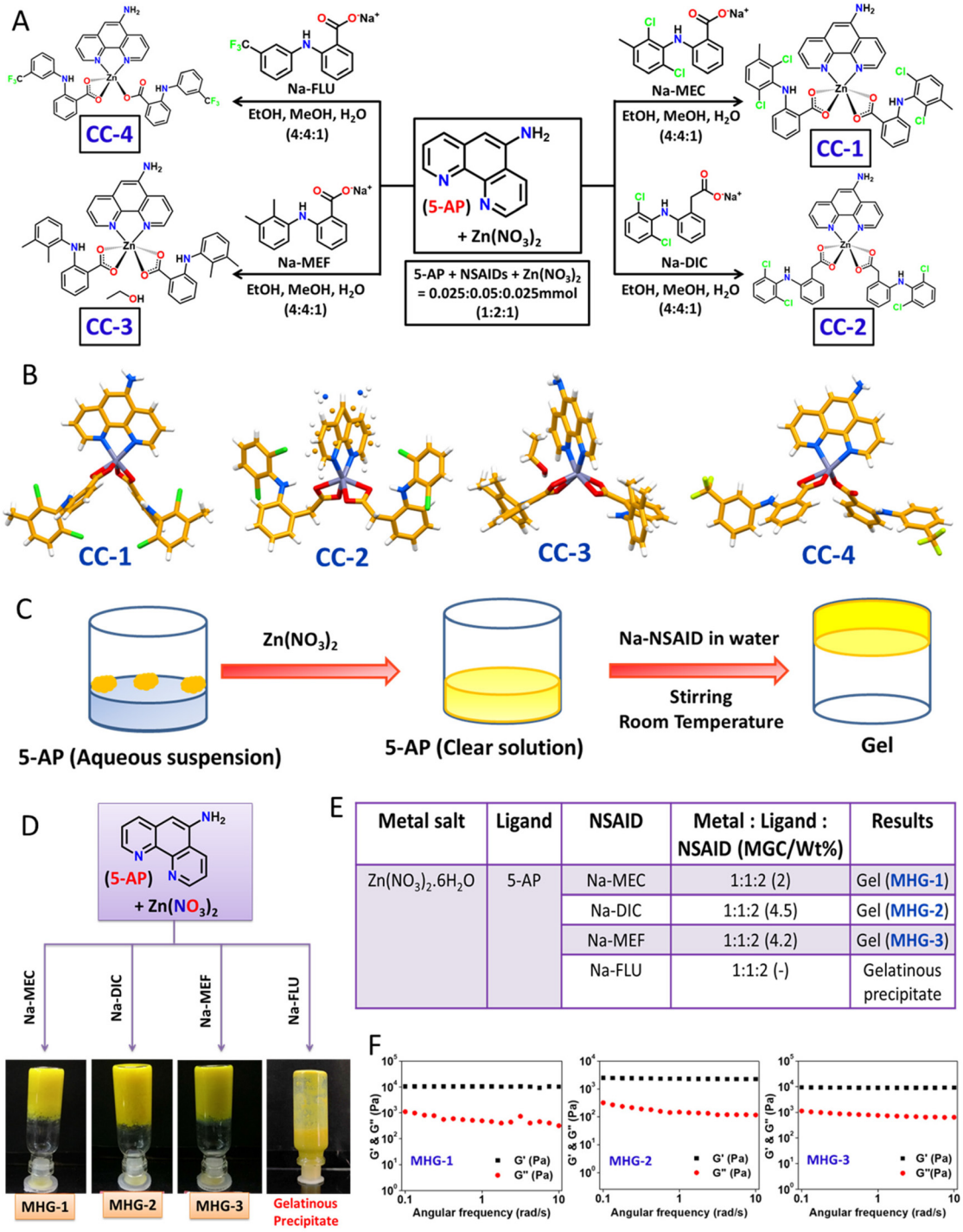

Metal salt	Ligand	NSAID	Metal : Ligand : NSAID (MGC/Wt%)	Results
$Zn(NO_3)_2.6H_2O$	5-AP	Na-MEC	1:1:2 (2)	Gel (MHG-1)
		Na-DIC	1:1:2 (4.5)	Gel (MHG-2)
		Na-MEF	1:1:2 (4.2)	Gel (MHG-3)
		Na-FLU	1:1:2 (-)	Gelatinous precipitate

Fig. 1 Synthesis of the CCs, hydrogel formation and characterization. (A) Synthetic route for the CCs. (B) Crystal structures of the CCs. (C) Schematic representation of the hydrogel preparation strategy. (D) Image of the inverted vials containing hydrogels. (E) Gelation data. (F) Dynamic rheology (frequency sweep, 8 wt% hydrogel).

O and amino N atoms. The lattice occluded solvate EtOH molecules connected these chains through O–H···O and N–H···O interactions, resulting in an overall 2D hydrogen bonded network, which was packed in a parallel manner along the *a*-axis (Fig. S4 and Table S5†). These results clearly suggested that both the ingredients (5-AP and NSAIDs) were successfully anchored to the Zn(II) metal centre with a precise stoichiometry of 1 : 2 : 1, and a pure crystalline product could be obtained. Powder X-ray diffraction (PXRD) data supported the crystalline phase purity of the synthesized CCs (Fig. S10†).

2.2 Hydrogelation

The self-assembly features involving both π–π stacking and hydrogen bonding present in these CCs raised hope of the possibility of hydrogel formation. However, none of the CCs were soluble in water at room temperature. Interestingly, addition of solid $Zn(NO_3)_2$ to an aqueous suspension of 5-AP resulted in a clear solution, suggesting effective coordination between 5-AP and Zn(II). To our delight, addition of aqueous solution of the corresponding Na-NSAID, followed by mechanical stirring, produced opaque yellow metallohydrogels (MHG-1, MHG-2 and MHG-3) at room temperature for **CC-1**, **CC-2** and **CC-3**, as evident from the tube inversion test; a gelatinous precipitate was obtained for **CC-4** (Fig. 1C and D). In these experiments, the molar ratio of the reactants was maintained as guided by the corresponding single crystal structures (Fig. 1E). It is noteworthy that instantaneous hydrogelation of the drug complexes at room temperature (contrary to the usual heat-cool treatment to obtain gels) is advantageous for SDD. Dynamic rheological studies were carried out to confirm the viscoelastic properties of the MHGs. Amplitude sweep experiments performed on the hydrogels (8 wt%) displayed the linear viscoelastic (LVE) region, which is typical of gel-like materials (Fig. S11†). Frequency sweep experiments, on the other hand, clearly established the viscoelastic properties of these hydrogels, as evident from the fact that the elastic modulus (G') was more than the loss modulus (G'') and remained frequency (ω s^{-1}) invariant especially in the longer time scale (Fig. 1F). All the hydrogels were found to be rheologically strong, as evident from the remarkable $\tan\delta$ values ranging 0.05–0.09 (Table S7†). The morphology of the dried hydrogels under TEM appeared to be colloidal aggregates (Fig. S12†). The absence of entangled fibrillar networks, *i.e.*, self-assembled fibrillar networks (SAFiNs),[55] typically observed for supramolecular gels, indicated that gelation did not take place *via* SAFiN formation in our case; rather, interactions involving the nanosized particles of the coordination complexes were responsible for the formation of gel networks.[56] Interestingly, the stretching frequency of the carboxylate of the Na-NSAID experienced a blue shift ($\Delta\nu$ = 5–78 cm^{-1}) in the corresponding xerogels, suggesting carboxylate–Zn coordination in the xerogels as well (Fig. S14 and Table S8†).

2.3 Rheoreversibility, tube-squeezing-out ability, long-term stability and injectability make MHG-1 suitable for real-life applications

Low $\tan\delta$ values from the frequency sweep experiments suggested that the gels were rheologically strong. Now, to use these hydrogels for local applications, they must possess good thixotropic properties. Interestingly, the hydrogels (8 wt%) showed good rheoreversibility over several low–high strain cycles during the thixotropic experiments (Fig. 2A). Not only that, during these studies, we noticed that the hydrogel MHG-1 (which had the least $\tan\delta$ value) showed good adhering properties on a glass surface (Fig. 2B), which was also found when a small amount of it was taken on fingers and was randomly moved (Fig. 2C and ESI movie 1†). This property might be an advantage for its topical use (Fig. 2D). Another important fact was the long-time stability of the hydrogel. For that reason, we kept MHG-1 (4 wt%, 1 mL) for 60 days at room temperature and under light exposure and air-tight conditions (Fig. 2E), and after that, evaluated the viscoelastic properties by frequency sweep experiments (Fig. 2F). The data suggested that the hydrogel had good viscoelastic properties, showing a remarkable $\tan\delta$ value (0.08) even after 60 days. We have also evaluated its squeezing property and injectability to use it in a more practical way. The data showed that the hydrogel could be squeezed out from a plastic tube and injection syringe without any phase separation, suggesting the hydrogel could become a potential candidate in topical as well as local applications for therapeutic use (Fig. 2G and H and ESI movies 2 and 3†).

2.4 Biological studies

2.4.1 *In vitro* cytotoxicity and anticancer assessment of the CCs: CC-1 is best suited. Having achieved this feat, *i.e.*, successful synthesis of hydrogelators containing a drug/active molecule (5-AP), we now set out to evaluate their suitability for SDD applications. For this purpose, we first carried out an MTT assay using these hydrogelators on a murine melanoma cell line B16-F10, which is known to serve as a human skin cancer model. The data suggested that **CC-1** had the best anticancer activity (IC_{50} = 0.025 mM) among the hydrogelators (Fig. 3A and S15†). On the other hand, cytotoxicity of **CC-1** turned out be the least (IC_{50} > 0.1 mM) against the murine macrophage cell line RAW 264.7 (Fig. 3B and S16†). Therefore, the MTT assay data suggested that **CC-1** was best suited for further studies. Interestingly, when we evaluated the anticancer ability of the ligands present in **CC-1**, *i.e.*, 5-AP and Na-MEC against B16-F10, we found out that 5-AP did not have appreciable anticancer activity, whereas Na-MEC at a concentration of ~0.2 mM could kill more than 50% cancer cells (Fig. S17†). It is interesting to note that nearly 10% cancer cells were killed by Na-MEC at a concentration of 0.05 mM, whereas the anticancer ability in its coordination complex form (**CC-1**) was nearly five times higher (note that the equivalent concentration of Na-MEC was 0.05 mM in 0.025 mM **CC-1** that killed nearly 50% cancer cells). Since we will be working with the hydrogel of **CC-1** for SDD application, we also compared the anticancer activity of both **CC-1** and its xerogel against B16-F10 and found that they were comparable (Fig. 3C and S18†). It is also important to evaluate the effect of **CC-1** on both murine muscle cell (C2C12) and horse skin cell (E. Derm (NBL-6)), considering its topical application in the final stage. The MTT assay data suggested that C2C12 cells could tolerate a significantly large concentration of **CC-1** (IC_{50} > 0.1 mM), whereas relatively less concentrated **CC-1** could kill more than 50% normal skin cells (IC_{50} < 0.025 mM) (Fig. S19†). MTT assays of the ligands (5-AP and Na-MEC) revealed that 5-AP was mainly responsible for the killing of normal skin cells (5-AP@IC_{50} < 0.023 mM; Na-MEC@IC_{50} > 0.2 mM) (Fig. S20†). The fact that **CC-1** did not adversely affect

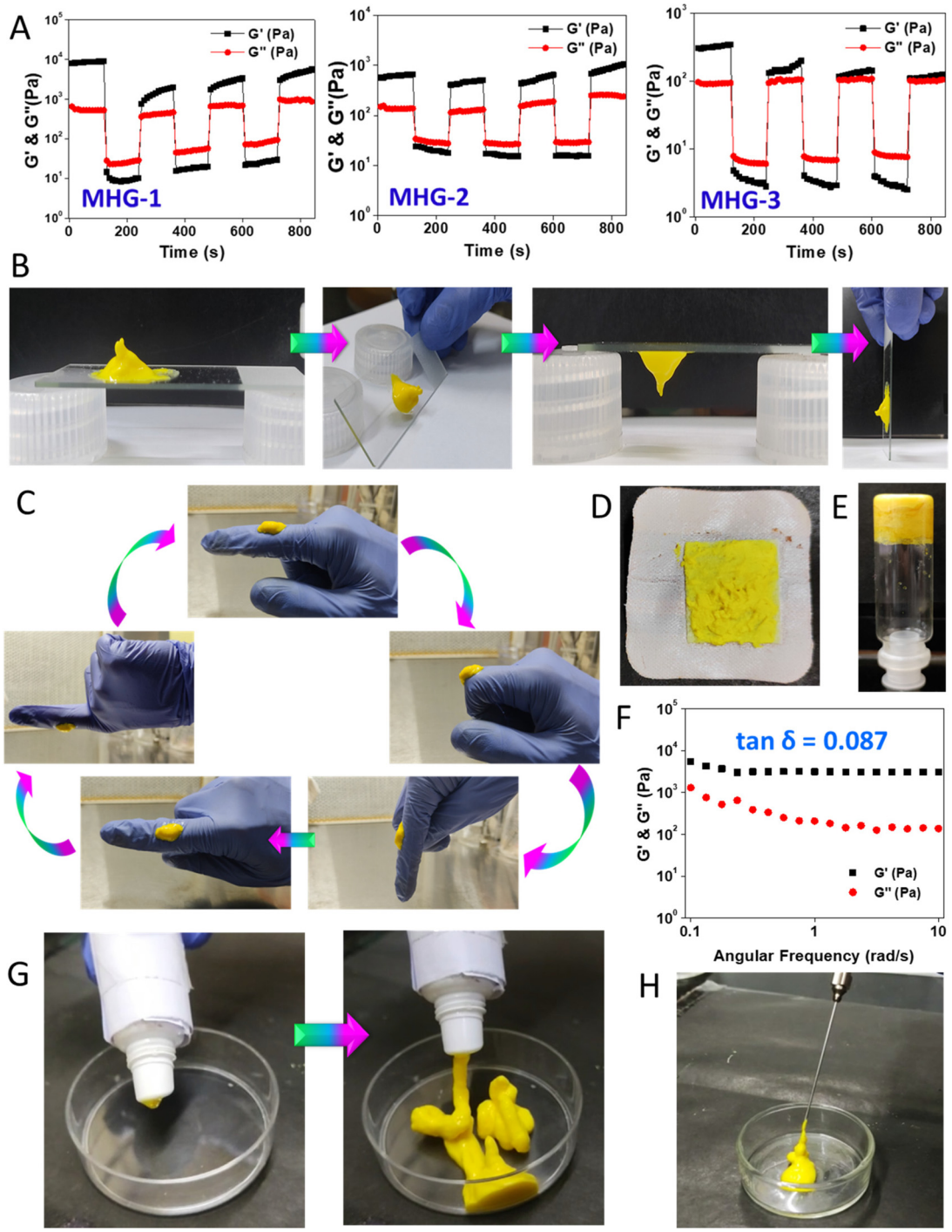

Fig. 2 Material properties of the hydrogel. (A) Rheoreversibility of the hydrogels (MHG-1, MHG-2 and MHG-3). (B and C) Adhering properties of MHG-1 (4 wt%). (D) A bandage pad containing MHG-1. (E and F) Image of the inverted vial and dynamic rheology (frequency sweep, 4 wt% hydrogel) of 60-day-old MHG-1. (G and H) Squeezing-out properties and injectability of MHG-1.

muscle cells and killed normal skin cells might be an advantage in its topical application, because when the hydrogel of **CC-1** will be implanted subcutaneously, it will not damage the muscle cells just beneath the hypodermis, whereas healing will be facilitated by killing normal skin cells around the tumor site. We have also carried out hemolysis experiments in order to find out the biocompatibility of **CC-1** on C57BL/6 mice; the data suggested that **CC-1** and its component ligands had good biocompatibility at a concentration range of 0.025–0.075 mM and 0.2 mM, respectively (Fig. 3D, E and S21†).

2.4.2 CC-1 localizes within the mitochondria and inhibits cancer cell migration *via* G1 phase arrest. To probe internaliz-

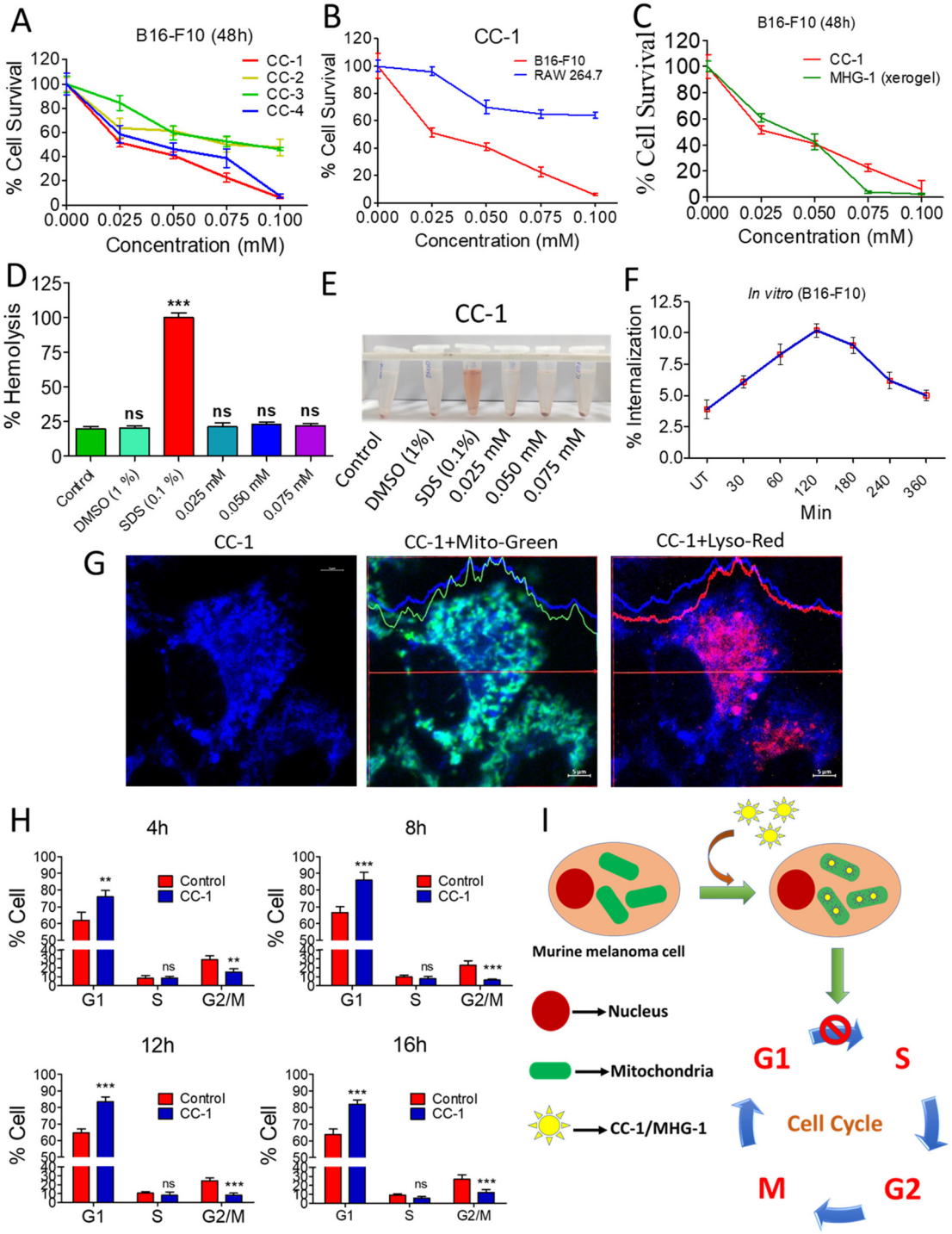

Fig. 3 Anticancer activity of **CC-1** on murine melanoma cells (B16-F10) under *in vitro* conditions. (A) MTT assay of the CCs against B16-F10 cells. (B) MTT assay of **CC-1** against RAW 264.7 and B16-F10 cells after 48 h. (C) MTT assay of **CC-1** and MHG-1 (xerogel) against B16-F10 cells after 48 h. (D) Hemolysis of **CC-1** on murine blood (all calculations were carried out by considering that 100% hemolysis occurred in the SDS-treated set; DMSO was used as the control solvent). (E) Image of **CC-1**-, SDS- and DMSO-treated murine blood after 3 h incubation. (F) % Internalization of **CC-1** (0.025 mM) in B16-F10 cells as per the flow cytometry data (see Fig. S23†) (UT – untreated cells). (G) LSCM images of **CC-1** (0.025 mM)-treated B16-F10 cells after 120 min incubation. Significant overlap of blue and green fluorescence due to **CC-1** internalization and MitoTracker™-stained mitochondria, respectively, and lack of that with red fluorescence due to the LysoTracker™-stained lysosome confirmed mitochondrial internalization of **CC-1** (scale bar = 5 μm). (H) Cell cycle analysis of **CC-1** (0.025 mM)-treated B16-F10 cells (see Fig. S28†). (I) Schematic representation of **CC-1** internalization and cell cycle arrest. In the line graphs, data are represented as mean ± SD (n = 3); bar graphs are represented as mean + SD (n = 3), where $^{**}p < 0.01$ and $^{***}p < 0.001$ and ns is non-significant.

ation of **CC-1** within the cancer cells (B16-F10), we systematically carried out flow cytometry and cell imaging studies using laser scanning confocal microscopy (LSCM). Fluorescence spectra of **CC-1** showed an intense peak at ~410 nm (λ_{ex} = 300 nm) (Fig. S22†). Therefore, flow cytometry data were collected using a blue filter (DAPI). It was observed that % cells having blue fluorescence gradually increased up to 120 min, indicating strong interactions of **CC-1** within the cancer cells (Fig. 3F and S23†). LSCM imaging carried out under various staining conditions clearly confirmed the internalization of **CC-1** as well as its subcellular localization in the mitochondria (Fig. 3G and S24†). It may be noted that after 120 min of incubation, % cells having blue fluorescence gradually decreased (Fig. 3F and S23†). Subsequently, LSCM images after 180 min of incubation with **CC-1** (0.025 mM) under propidium iodide (PI) staining showed a leaky cell membrane facilitating excretion of **CC-1** from the cancer cells (Fig. S25†). Having established that **CC-1** was indeed internalized within the cancer cells, we then tried to understand its intracellular role. For this purpose, we incubated B16-F10 cells with **CC-1** (0.025 mM) for 48 h at 37° C in a CO_2 incubator under different staining conditions (HO33342 and PI). In the control set of the experiments, the nuclei were found to be homogeneously stained with HO33342 with no red fluorescence due to PI, suggesting a healthy cell morphology, whereas in the treated cells, nuclear condensation/fragmentation was observed in the HO33342-stained cells and rupture of the cell membrane was evident from the red fluorescence on the condensed/fragmented nuclei (Fig. S26†). We further evaluated the anticancer properties of **CC-1** by a scratch assay[57,58] on B16-F10 cells. It was observed that with respect to the control and Na-MEC, the migration speed of cells was significantly reduced, clearly establishing the anticancer activity of **CC-1** (Fig. S27†). Cell cycle analyses were performed in order to gain further insights into the reason behind the inhibited cell migration in the scratch assay. Flow cytometry data of the control and treated cells (B16-F10 treated with 0.025 mM **CC-1**) recorded at various time intervals revealed that cell arrest took place in the G1 phase (Fig. 3H and S28†). These data clearly indicated that the reduced cell migration speed under the influence of **CC-1** was due to the cell arrest in the G1 phase (Fig. 3I). Nuclear condensation/fragmentation along with inhibition of cell migration by G1 phase arrest in the cell cycle is a clear indication of apoptosis.[59–61]

2.4.3 Anticancer activity of the hydrogel (MHG-1) under *in vivo* conditions. The *in vitro* data discussed thus far clearly indicated that **CC-1** did possess significant anticancer activity against B16-F10 and it also could kill normal skin cells leaving the muscle cells unaffected. These data encouraged us to further evaluate the anticancer activity of MHG-1 on an orthotropic melanoma tumor model in C57BL/6 mice (see the Experimental section for details). B16-F10 cells were intradermally injected to C57BL/6 mice to generate tumors. After the tumors were grown for seven days, the hydrogel at various concentrations (2, 4 and 8 wt%) was implanted just below the tumor by subcutaneous injection (single dose during the 21-day study period) and the tumor volume was measured daily for the study period (Fig. 4A). Interestingly, tumor growth was nearly arrested in the treated mice, indicating the antitumor activity of the hydrogel (Fig. 4B, C and S29†), whereas the tumor volume in the control set gradually increased as expected. After 21 days, the mice were sacrificed and the weight of the tumors was measured; with respect to control, the weight of the tumors in the treated group was significantly reduced (Fig. 4D and S30†). It may be noted that in two sets of the treated mice, the tumors were completely eradicated, whereas in the case of a known anticancer drug-treated mice (5-fluorouracil or 5-Fu; here also a single dose was injected as PBS suspension at the tumor site during the 21-day study period), inconsistent results including death of the mice were observed (Fig. 4B and S30†). It may be worth mentioning here that we observed no significant change of body weight of the mice during the experiment period of 21 days, indicating no apparent toxicity due to the hydrogel application (Fig. 4E). We have also monitored the control and treated mice for a duration of 32 weeks in order to assess the reoccurrence of tumors and also survivability (Fig. 4F). It was observed that, in the control set, no mice survived after 7 weeks, whereas the survivability of the 4 and 8 wt% treated mice was 20% even after 32 weeks, with no reoccurrence of tumors (Fig. 4G and H and ESI movie 4†). However, no mice survived in the 2 wt% treated set after 21 weeks (Fig. 4G). Further *in vivo* experiments carried out with an equivalent amount of the components (5-AP, Na-MEC and $Zn(NO_3)_2$) present in a 4 wt% hydrogel revealed that both Na-MEC and 5-AP could reduce tumor growth, whereas $Zn(NO_3)_2$ had an insignificant effect on the tumors (Fig. S31 and S32†). However, the health of the mice treated with Na-MEC appeared to be weak, which was also reflected through their reduced body weight (Fig. S32C†). These data clearly suggested that the active ingredients of the hydrogel must have been internalized in order for it to act as an anticancer agent. In fact, experiments carried out by monitoring the λ_{max} of 5-AP of the PBS supernatant kept on a hydrogel bed (at MGC) with time confirmed its leaching to the bulk solvent (Fig. 4I). An LC-MS study of the supernatant collected after 48 h suggested the release of both the components from the hydrogel. Furthermore, the data clearly showed that nearly 40% of the drug (MEC) was released from the gel bed after 48 h (Fig. S50†). Thus, it is reasonable to conclude that both the active ingredients leached out from the subcutaneously injected hydrogel at the tumor site and the observed anticancer activity of the hydrogel could be rationalized. The fact that 5-AP was actually being internalized within the cancer cells was further supported by the flow cytometry data from a single cell suspension of tumor tissues treated with various concentrations of the hydrogel (Fig. S33†). These data corroborated well with the results obtained *in vitro* (Fig. 3F and S23†).

In vitro cell migration and cell cycle data revealed the inhibition of cancer cell proliferation after the treatment. As Ki-67 is upregulated in any proliferative cells such as cancerous cells,[62] we incubated the tumor tissue collected after 21 days of the treatment with 4 wt% hydrogel with an anti-Ki-67 mono-

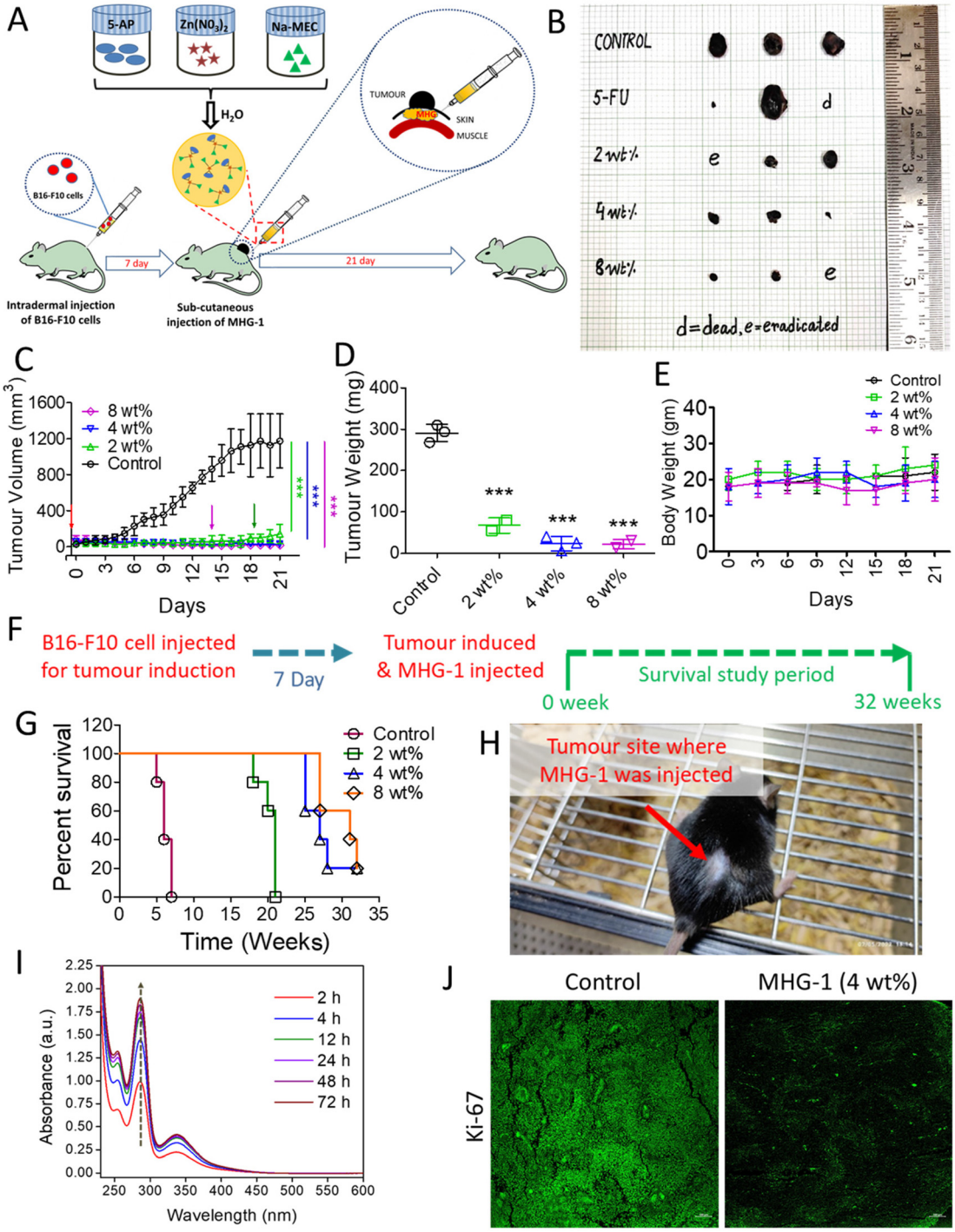

Fig. 4 *In vivo* anticancer activity of MHG-1 and its *in vitro* release. (A) Schematic representation of the overall *in vivo* procedure. (B) The size of the tumors under various conditions. (C) Tumor volume (mm^3) during the treatment period (21 days). Tumor eradication was noticed in 2 (green arrow) and 8 wt% (magenta arrow) MHG-1 treated mice after 18 and 14 days, respectively. Note that each group contained three mice and tumor eradication was observed in one mouse in both cases (2 and 8 wt%). The red arrow indicates the day at which the hydrogel was implanted. (D) Tumor weight after the 21-day MHG-1 treatment. (E) Body weight of the tumor bearing mice treated with MHG-1 during the treatment period (21 days). (F) Strategy for the survival study. (G) Survivability plot of the MHG-1 treated mice for 32 weeks. (H) Image of MHG-1 (4 wt%)-treated melanoma bearing mice after 32 weeks. The image shows complete eradication of the tumor after MHG-1 treatment. The red arrow indicates the tumor site, where MHG-1 was injected. (I) Time-dependent UV-vis spectrum of the released component from the MHG-1 bed (prepared in PBS) (the dashed arrow represents an increase in absorption of the leached out supernatant solution with time). (J) The LSCM image of the anti-Ki-67 monoclonal antibody-stained tumor tissue treated with MHG-1 (4 wt%). The tumor was excised after 21 days of MHG-1 treatment. Reduced Ki-67 expression (low-intensity green fluorescence compared to the control) was observed after MHG-1 treatment (scale bar = 100 μm). In the graphs, data are represented as mean ± SD (n = 3); where ***p < 0.001.

clonal antibody. It was clear from the LSCM images that the expression of Ki-67 was greatly reduced in the treated tissues as compared to the control, thereby supporting the role of the hydrogel as an anticancer agent (Fig. 4J and Fig. S51†).

2.4.4 *In vitro* and *in vivo* results suggested apoptosis. The above discussions suggest that apoptosis might be the main cause for cancer cell death. To further confirm, an annexin V-FITC/PI assay was carried out on B16-F10 cells treated with varying concentrations of **CC-1** (0.025, 0.05 and 0.075 mM). Binding of extracellular phosphatidyl serine present in apoptotic cells with the antibody annexin V-FITC producing green fluorescence and PI positive cells producing red fluorescence was evident from the flow cytometry data, confirming the onset of apoptosis (Fig. 5A). The results were further confirmed by the LSCM images under various staining conditions with HO33342, annexin V-FITC and PI (Fig. 5B and S34†). The effect of **CC-1** on B16-F10 cells was also evident from the deformed morphology of the cells observed using a cryo-TEM and optical microscope (Fig. 5C and S35†). SEM images of the treated cells also showed significant shrinkage of the cells along with apoptotic blebs, supporting the onset of apoptosis (Fig. 5D and S36†). The *in vivo* experiments also supported the apoptotic pathway; annexin V-FITC/PI-stained single cell suspension of the hydrogel-treated tumor tissues in flow cytometry showed the onset of apoptosis (Fig. S37†); LSCM images of the hydrogel-treated tumor tissues under annexin V-FITC staining conditions also supported apoptosis (Fig. 5E and Fig. S52†).

Apoptosis was also evident from the mitochondrial membrane potential (MMP) assay with JC-1 in B16-F10 cells treated with **CC-1** in a dose-dependent manner; a gradual increase of green fluorescence with an increase in the concentration of **CC-1** in flow cytometry clearly indicated depolarization of MMP, supporting apoptosis (Fig. 5F). It was also confirmed by the LSCM images of B16-F10 cells under various staining conditions (Fig. 5G). Flow cytometry data from a single cell suspension from the hydrogel-treated tumor tissues also supported apoptosis, as evident from the JC-1 assay (Fig. S38†). Thus, our findings from both *in vitro* and *in vivo* studies clearly suggested that **CC-1** (*in vitro*)/MHG-1 (*in vivo*) triggers apoptosis on the cancer cells *via* MMP depolarisation (Fig. 5H).

Finally, we were able to record a video, where cells were triggering apoptosis after treatment with **CC-1** (concentration: 10 times higher than IC_{50}) using a confocal microscope. The video clearly demonstrated the internalization of **CC-1**-induced apoptotic bleb formation, with notable morphological changes (Fig. 6 and ESI movie 5†).

2.4.5 CC-1/MHG-1 kills side population cells both *in vitro* and *in vivo*

Hoechst efflux assay. Drug resistance to chemotherapy and tumor reoccurrence are common in cancer treatment, which is primarily due to side population (SP) cells having cancer stem cell-like properties.[63,64] Efflux of chemotherapeutic drugs by SP cells can be monitored by the efflux of HO33342, which produces red fluorescence. Decreasing red fluorescence in the flow cytometry data from B16-F10 cells treated with verapamil (a well-known drug that kills SP cells, as the positive control) and **CC-1** with varying concentrations clearly supported the ability of **CC-1** in killing SP cells (Fig. S39†). Similar experiments performed on a single cell suspension of the hydrogel-treated tumor tissues also supported the *in vitro* data (Fig. S40†).

2.4.6 CC-1/MHG-1 reduces oxidative stress both *in vitro* and *in vivo*. Homeostatic balance of normal cells is largely controlled by intracellular reactive oxygen species (ROS), whereas its excessive accumulation is observed in cancer cells.[65] ROS scavenging properties of NSAIDs are well known,[66] which understandably reduces the supply of essential oxygen to growing cancer cells, consequently leading to apoptosis.[67] Therefore, we carried out flow cytometry on B16-F10 cells treated with **CC-1** under DCFDA staining conditions in a time-dependent manner. DCFDA produces DCF, showing green fluorescence when reacted with ROS. A gradual decrease of green fluorescence in the flow cytometry data clearly suggested the scavenging properties of the constituent NSAID component (MEC) present as a ligand in the hydrogelator (Fig. S41†). Once again, the *in vivo* studies carried out on a single cell suspension of the hydrogel-treated tumor tissues led to a similar conclusion (Fig. S42†).

2.4.7 Histopathology: MHG-1 was found responsible for nuclear condensation/fragmentation, inhibited angiogenesis and monocyte infiltration. To gain further insights of the hydrogel treatment on the tumor tissues, we carried out histopathological studies. Hydrogel-treated and untreated (control) tumor tissues under Hematoxylin and Eosin (H&E) staining conditions were subjected to histopathology. The photomicrographs of the H&E-stained tissues clearly revealed the existence of characteristic apoptotic nuclear condensation/fragmentation, monocyte infiltration indicating the pro-inflammatory immune response and significant loss of blood vessels indicating inhibition of angiogenesis leading to cancer cell death (Fig. 7A–D and S43†). Immunofluorescence staining of tumour tissues with the vascular endothelial cell marker CD31 also suggested loss of blood vessels after MHG-1 treatment (Fig. S53†). Interestingly, histopathology (H&E) of the skin tissues collected from the peripheral region of the tumor site showed extensive vacuolization in the tissues treated with the hydrogel, whereas the non-treated tissues showed characteristic healthy features (Fig. S44†). These data also supported the *in vitro* studies on skin cells (E. Derm (NBL-6)) (see above). We have also carried out histopathological studies of some randomly collected tissues from various organs (liver, kidneys, lungs, heart and spleen) from the hydrogel-treated mice and found that all of them showed characteristic healthy features, indicating no apparent toxicity due to the hydrogel treatment (Fig. S45†), which is an obvious advantage of local chemotherapy.

2.4.8 *In vivo* experiments suggest that MHG-1 effectively modulates the anti-tumor immune system in the tumor microenvironment. The immune system in the tumor microenvironment plays a crucial role in tumor inhibition/

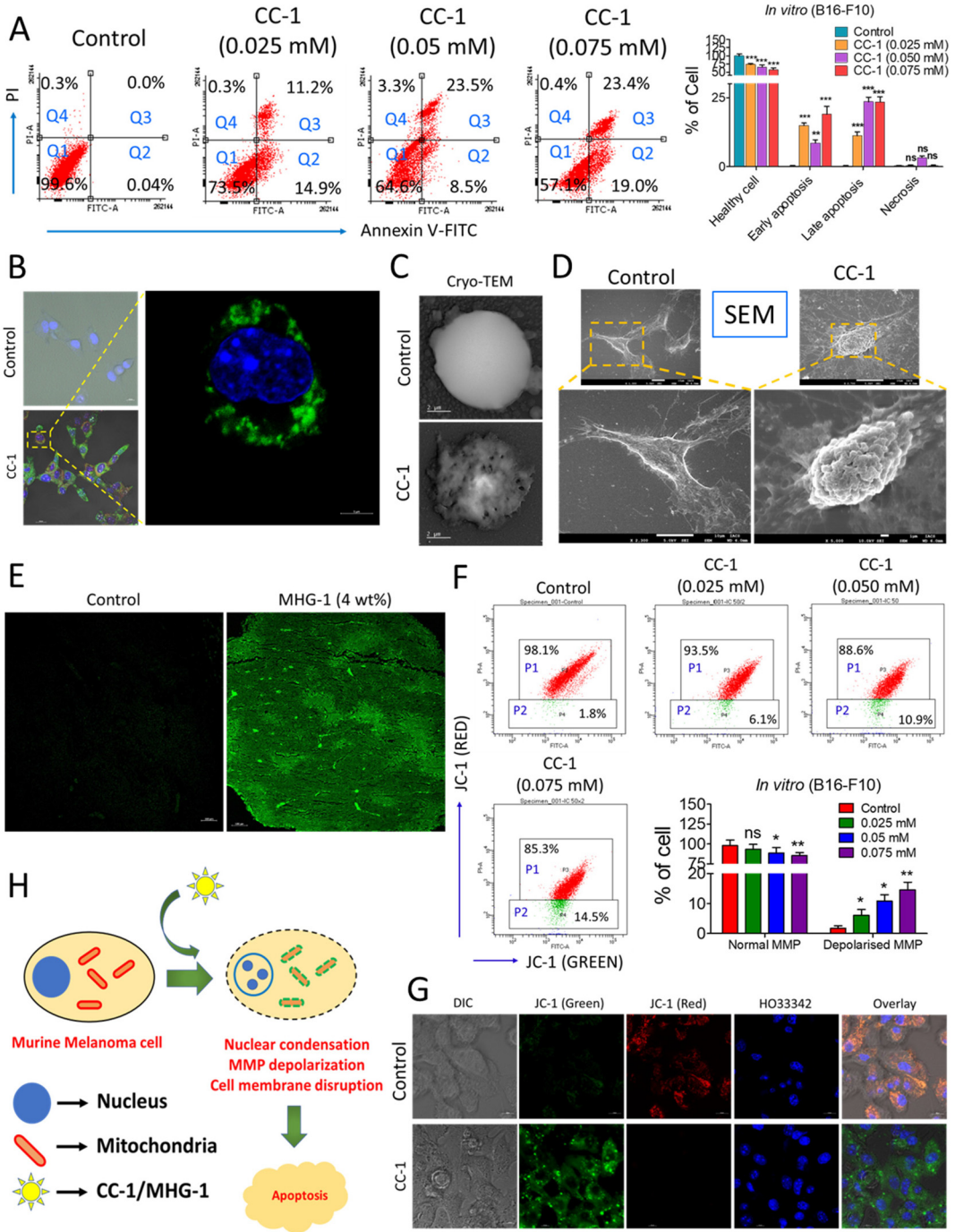

Fig. 5 Probing the onset of apoptosis with **CC-1**/MHG-1 in murine melanoma cells (A) Flow cytometry of **CC-1**-treated B16-F10 cells, after 48 h incubation (Q1-healthy cells; Q2-early apoptosis; Q3-late apoptosis; Q4-necrosis). (B) Part of the LSCM images of **CC-1** (0.025 mM)-treated B16-F10 cells depicted in Fig. S34,† highlighting the onset of apoptosis as revealed from the green fluorescence arising due to annexin V-FITC binding with the extracellular phosphatidyl serine (scale bar = 20 μm). (C and D) Cryo-TEM and SEM images of a single B16-F10 cell under treated (**CC-1**/0.025 mM) and untreated (control) conditions after 48 h (scale bar = 2 μm and 10 μm), respectively. (E) The LSCM image of untreated and MHG-1 (4 wt%)-treated tumor tissues stained with annexin V-FITC. The tumor was excised after 21 days of MHG-1 treatment. Increased green fluorescence arising due to annexin V-FITC binding with the extracellular phosphatidyl serine supported apoptosis in *in vivo* as well (scale bar = 100 μm). (F) Flow cytometry of **CC-1**-treated B16-F10 cells stained with JC-1 after 48 h. Increased cell population emitting green fluorescence (P2) indicated MMP depolarization, supporting apoptosis. (G) LSCM images of **CC-1** (0.025 mM)-treated B16-F10 cells stained with JC-1 after 48 h. Distinct green fluorescence in the overlay image of the treated cells suggested MMP depolarization, supporting apoptosis (scale bar = 10 μm). (H) Schematic representation of the mechanism of cancer cell death. In the graphs, data are represented as mean + SD (n = 3), where *p < 0.05, **p < 0.01 and ***p < 0.001 and ns is non-significant.

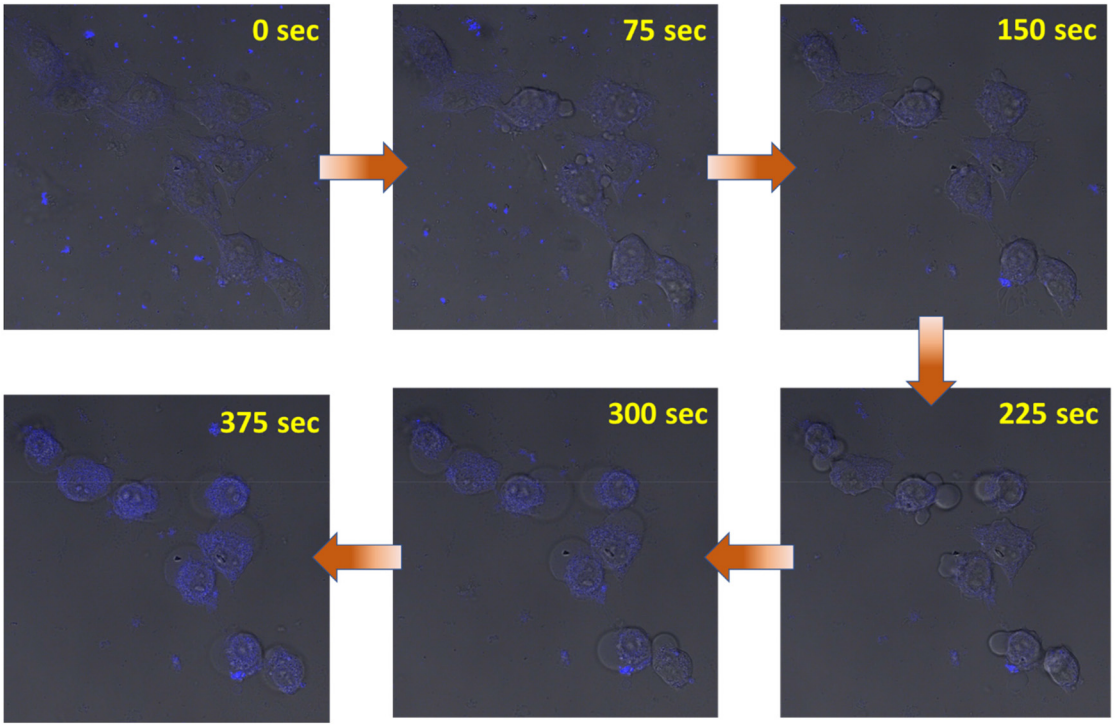

Fig. 6 Internalization of **CC-1** (blue) triggering apoptosis.

progression.[68–70] Macrophages in the tumor microenvironment direct the fate of tumors.[71] Previous studies revealed that M2 macrophages potentially induced tumor growth; on the other hand, M1 macrophages showed anti-tumor properties.[72–74] NSAIDs are cyclooxygenase (COX) inhibitors that help to reduce the intracellular concentration of PGE_2, which plays an important role in immunomodulation.[58,75] An increased PGE_2 level in the tumor microenvironment often plays an important role in tumor progression and metastasis.[76,77]

Since the hydrogel under study contained a NSAID component, namely MEC, and since it showed encouraging results as an anticancer agent triggering apoptosis as revealed by various *in vitro* and *in vivo* experiments including inhibition of angiogenesis and a sign of a pro-inflammatory immune response in the histopathological studies (see above), we decided to investigate the intracellular PGE_2 level and the status of the immune system in the tumor microenvironment after the hydrogel treatment. The PGE_2 assay carried out on inflamed RAW 264.7 cells (LPS treated) showed significant reduction of PGE_2 concentration when treated with **CC-1** and Na-MEC, indicating the well-known role of NSAIDs in PGE_2 reduction present in **CC-1** (Fig. S46†). Similar results were also obtained for the hydrogel-treated tumor and skin tissues, suggesting the effective role of reducing PGE_2 due to subcutaneous administration of the hydrogel (Fig. 7E and S47†).

The reduction in PGE_2 expression in the tumor microenvironment often changes the cytokine secretions, which could exert anti-tumor activity.[78] Furthermore, it is well known that PGE_2 inhibits IFN-γ production and opposes IL-12 signalling by proliferating Th2 lymphocytes.[78] Thus, we investigated IFN-γ and IL-12 contents in the tumor microenvironment after the treatment. The flow cytometry data suggested induction in IFN-γ as well as IL-12 expression after 9 and 18 days of the hydrogel treatment with respect to that of the control (Fig. 7F, S48 and S49†). The overexpression of IFN-γ in the tumor microenvironment indicated an increase in M1 macrophage population.[71] Furthermore, IFN-γ from Th1 cells recruits and maintains the M1 phenotype of macrophages; on the other hand, IL-12 from M1 macrophages recruits and maintains the Th1 phenotype.[79] In our case also, simultaneous overexpression of IL-12 along with IFN-γ was observed. Thus, it may be an indication of maintenance and recruitment of Th1 lymphocytes and M1 macrophages. To further confirm this, we checked the expression of other pro-inflammatory cytokines (TNF-α, IL-2 and IL-6) related to Th1 lymphocytes and M1 macrophages. The data depict an increased cytokine expression after the hydrogel treatment (Fig. 7F, S48 and S49†). These results suggested an increased M1 population in the tumor microenvironment. It is noteworthy that IL-2 or its combination with drug/other cytokines is used as subcutaneous/intravenous injection in melanoma immune therapy.[80,81] Furthermore, IL-2 not only showed regression of metastatic melanoma, but also could be a useful immunotherapy for tumor eradication. Due to the short serum half-life of IL-2, it faces several limitations.[82] In our case, the hydrogel itself is able to induce IL-2 concentration locally without any notable side effects. In addition, in some of the cases, we have observed complete era-

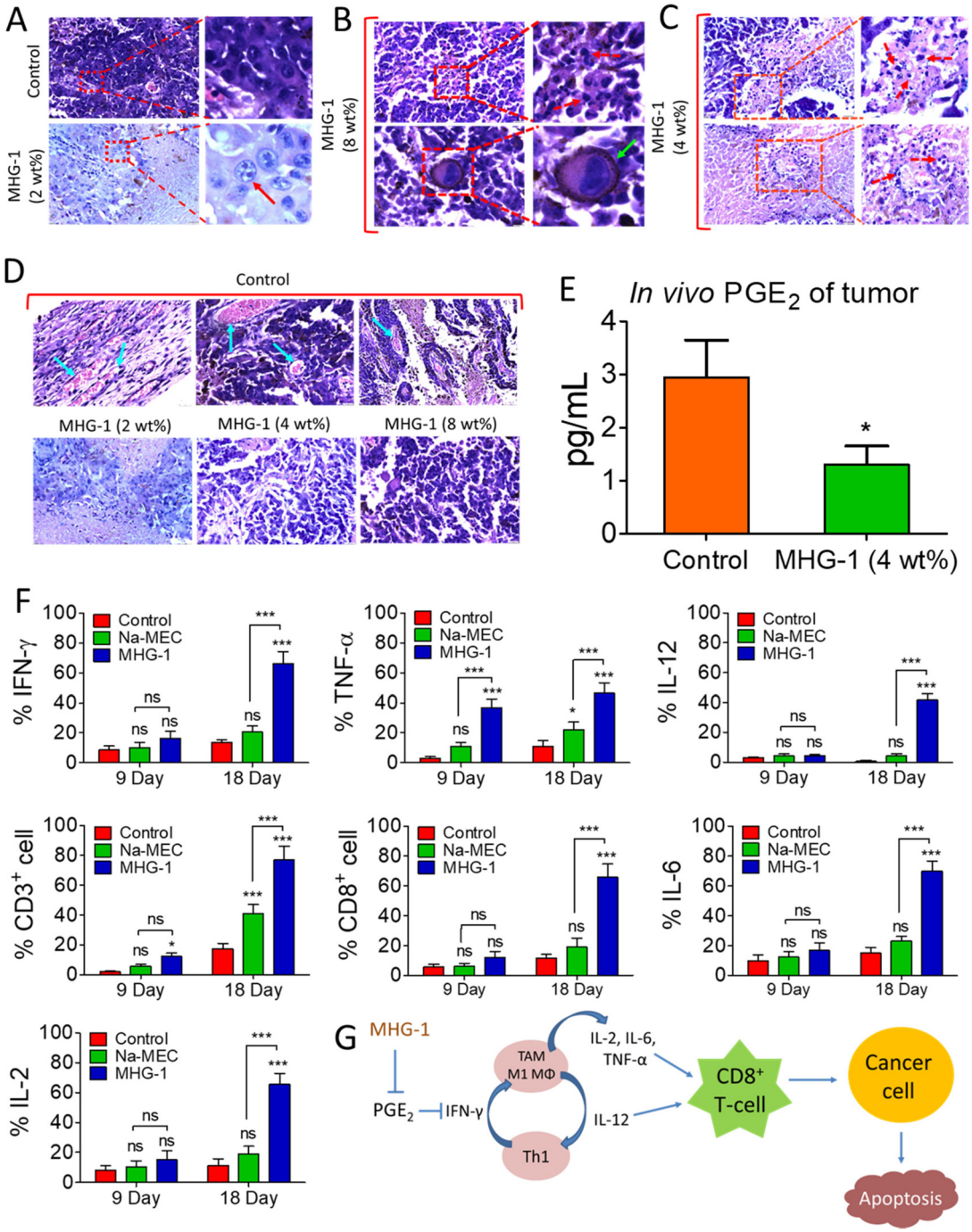

Fig. 7 Optical microscopic images of the H&E-stained tumor tissue (the tumor was excised after the 21-day MHG-1 treatment) and immunomodulation in the tumor microenvironment with MHG-1. (A) The intense blue dots within the nuclei (red arrow) suggest nuclear condensation/fragmentation (scale bar = 20 μm). (B) The giant cell with lobular or kidney shaped nuclei (green arrow) suggests monocyte infiltration in the tumor (scale bar = 10 μm). (C) The blue dots (red arrow dashed line) within the cell suggest nuclear fragmentation (scale bar = 20 μm). (D) The light blue arrows suggest the presence of blood vessels in the control set. In contrast, in the MHG-1-treated tumor tissue, blood vessels were absent (scale bar = 20 μm). (E) PGE_2 assay of the tumor tissue supernatant after 18 days of MHG-1 (4 wt%) treatment. (F) Graphical representation of pro-inflammatory cytokine expression and T-cell populations in the tumor microenvironment, after MHG-1 (4 wt%) treatment. Data were obtained from flow cytometry. (G) Schematic representation of the MHG-1-induced immunoediting mechanism in the tumor microenvironment, leading to cancer cell apoptosis. In the graphs, data are represented as mean + SD (n = 3), where *p < 0.05 and ***p < 0.001 and ns is non-significant.

dication of the tumors. It is well known that cytokines (IL-12, IL-6, TNF-α and IL-2) are directly/indirectly responsible for the maturation and activation of cytotoxic T cells ($CD8^+$ cells), which interact with cancer cells, triggering apoptosis/necrosis.[79] Thus, we investigated T cell populations in the hydrogel-treated tumor microenvironment. Our data suggested an increase in total T cell population ($CD3^+$ cells), indicating expansion of tumor infiltrating T cells as well as cytotoxic T cell population ($CD8^+$ cells) (Fig. 7F, S48 and S49†).

In summary, the subcutaneously injected hydrogel potentially reduces PGE_2 expression, which in turn induces IFN-γ and IL-12. IFN-γ and IL-12 recruited M1 macrophages and Th1 lymphocytes, which secreted pro-inflammatory cytokines (IL-12, IL-6, TNF-α and IL-2). Further, the pro-inflammatory cytokines activated the cytotoxic T cells ($CD8^+$ cells). Finally, the activated T cells ($CD8^+$ cells) interacted with the cancer cells, triggering apoptosis (Fig. 7G).

3 Conclusion

A series of Zn(II) coordination complexes derived from NSAIDs and 5-AP were designed, synthesized and crystallographically characterized for developing a self-drug-delivery system as hydrogels for treating the most fatal type of skin cancer (melanoma). One such hydrogel having MEC as the NSAID component, when subcutaneously implanted as a single dose, showed promising results in inhibiting melanoma-induced tumor growth in C57BL/6 mice, including complete eradication of tumors in some cases. Both *in vitro* and *in vivo* results suggested that MEC being a NSAID effectively reduced the intracellular PGE_2 concentration, thereby upregulating IFN-γ and IL-12, which in turn modulated the immune microenvironment of the tumor site by recruiting M1 macrophages and Th1 lymphocytes. Consequently, the secreted pro-inflammatory cytokines (IL-12, IL-6, TNF-α, IL-2) activated cytotoxic T cells ($CD8^+$), which eventually triggered apoptosis. The results presented herein highlight the following merits:

(a) Simple coordination chemistry and the concept of supramolecular chemistry have been employed to design hydrogels as a potential self-drug-delivery system for melanoma therapy. The absence of the need for a drug delivery vehicle usually required in a gel-based therapy understandably eliminates the concerns pertaining to drug loading and its effective release to the target site.

(b) The successful preparation of a stable and injectable hydrogel allows us to implant it to the tumor site *via* the subcutaneous route. The usual topical gel formulation in treating melanoma (*e.g.*, 5-fluorouracil loaded gel formulation) suffers from inefficient delivery of the anticancer drug to the cancer cells due to spreading and drying issues of the applied gel. However, the subcutaneous route (as it is implanted below the tumor) prevents both spreading and drying, thereby helping in maintaining high local concentration of the drug and its sustained release to the target site.

(c) Both *in vitro* and *in vivo* data strongly support that the all-in-one self-drug-delivery system thus developed is capable of providing both chemo- and immunotherapy to combat melanoma, as evident from the decreased intracellular PGE_2 level and up-regulation of IL-2. It is noteworthy that immunotherapy wherein the immune cytokine IL-2 is injected intravenously suffers from its short half-life and severe side effects.

The overall work reported in this paper is schematically depicted in Fig. S54.† The approach of developing a self-drug-delivery system by implanting a supramolecular drug-derived hydrogel to deliver chemotherapeutic agents along with an immunomodulator to combat melanoma is expected to open up new avenues in cancer therapy.

Author contributions

S. B. performed the synthesis, characterization, gelation, rheology, SXRD, PXRD, MTT, and scratch assay and performed all biological experiments along with and under the supervision of H. K. D. and P. D. conceptualized and supervised the project, analyzed the results, and co-wrote the manuscript with input from all the co-authors.

Conflicts of interest

The authors declare no competing interests.

Acknowledgements

P. D. thanks SERB (CRG/2019/000790) for the financial support. S. B. thanks UGC for SRF and H. K. D. thanks IACS for the RA fellowship. The authors thank Chanchal K. Das and Debapriya Ghatak for helping in flow cytometry and LSCM data collection. The authors also thank Dr Amitava Sengupta, Cancer Biology Division, CSIR-Indian Institute of Chemical Biology, Kolkata for gifting the PE-CF594 rat anti-mouse CD31 antibody. S. B. and H. K. D. thank Dr Poulami Chakraborty and Dr Protap Biswas for their continuous help and support. S. B and H. K. D. also thank Subhra Sankar Dutta for the help during LC-MS data collection. S. B. thanks Prosenjit Bera for the help in graphic designing. SXRD data were collected in the DBT-funded X-ray diffraction facility under the CEIB program at the School of Chemical Sciences, IACS, Kolkata. The animal experiments were performed under the ethical permission of Institutional Animal Ethics Committee (IAEC) having approval no. IACS/IAEC/2021-02 and were conducted following the IAEC guidelines.

References

1 https://www.who.int/health-topics/cancer#tab=tab_1.
2 https://www.iarc.who.int/news-events/global-burden-of-cutaneous-melanoma-in-2020-and-projections-to-2040/.

3 F. Danhier, O. Feron and V. Preat, *J. Controlled Release*, 2010, **148**, 135–146.
4 J. Fang, H. Nakamura and H. Maeda, *Adv. Drug Delivery Rev.*, 2011, **63**, 136–151.
5 T. Lammers, F. Kiessling, W. E. Hennink and G. Strom, *J. Controlled Release*, 2012, **161**, 175–187.
6 L. Cai, S. Liu, J. Guo and Y. G. Jia, *Acta Biomater.*, 2020, **113**, 84–100.
7 S. Khajouei, H. Ravan and A. Ebrahimi, *Adv. Colloid Interface Sci.*, 2020, **275**, 102060.
8 M. G. Raucci, U. D'Amora, A. Ronca and L. Ambrosio, *Adv. Funct. Mater.*, 2020, **9**, 2000349.
9 S. Y. Lee, M. Yang, J. H. Seo, D. I. Jeong, C. Hwang, H. J. Kim, J. Lee, K. Lee, J. Park and H. J. Cho, *ACS Appl. Mater. Interfaces*, 2021, **13**, 2189–2203.
10 J. Qi, T. Ding, T. Liu, X. Xia, S. Wu, J. Liu, Q. Chen, D. Zhang and H. Zhao, *Adv. Funct. Mater.*, 2022, **32**, 2204273.
11 F. Wang, H. Su, D. Xu, M. K. Monroe, C. F. Anderson, W. Zhang, R. Oh, Z. Wang, X. Sun, H. Wang, F. Wan and H. Cui, *Biomaterials*, 2021, **279**, 121182.
12 F. Ding, Q. Mou, Y. Ma, G. Pan, Y. Guo, G. Tong, C. H. J. Choi, X. Zhu and C. Zhang, *Angew. Chem., Int. Ed.*, 2018, **57**, 3064–3068.
13 H. Wang, Z. Feng, Y. Qin, J. Wang and B. Xu, *Angew. Chem., Int. Ed.*, 2018, **57**, 4931–4935.
14 L. Zhou, W. Pi, M. Hao, Y. Li, H. An, Q. Li, P. Zhang and Y. Wen, *Biomater. Sci.*, 2021, **9**, 4904.
15 N. Liu, S. Wu, X. Tian and X. Li, *J. Mater. Chem. B*, 2022, **10**, 5165.
16 J. Kim, D. M. Francis, L. F. Sestito, P. A. Archer, M. P. Manspeaker, M. J. O'Melia and S. N. Thomas, *Nat. Commun.*, 2022, **13**, 1479.
17 B. Wang, J. Chen, J. S. Caserto, X. Wang and M. Ma, *Nat. Commun.*, 2022, **13**, 3821.
18 C. Song, H. Phuengkham, Y. S. Kim, V. V. Dinh, I. Lee, I. W. Shin, H. S. Shin, S. M. Jin, S. H. Um, H. Lee, K. S. Hong, S.-M. Jin, E. Lee, T. H. Kang, Y.-M. Park and Y. T. Lim, *Nat. Commun.*, 2019, **10**, 3745.
19 R. G. Weiss, *J. Am. Chem. Soc.*, 2014, **136**, 7519–7530.
20 P. Dastidar, *Chem. Soc. Rev.*, 2008, **37**, 2699–2715.
21 P. Dastidar, *Gels*, 2019, **5**(1), 15.
22 S. Bonardd, B. Maiti, S. Grijalvo, J. Rodríguez, H. Enshaei, G. Kortaberria, C. Alemán and D. Díaz Díaz, *Soft Matter*, 2022, **18**, 4963–4972.
23 M. Samateh, S. Marwaha, J. K. James, V. Nanda and G. John, *Carbohydr. Res.*, 2022, **521**, 108647.
24 M.-O. M. Piepenbrock, G. O. Lloyd, N. Clarke and J. W. Steed, *Chem. Rev.*, 2010, **110**, 1960–2004.
25 Q. Wei and S. L. James, *Chem. Commun.*, 2005, 1555–1556.
26 J. H. van Esch and B. L. Feringa, *Angew. Chem., Int. Ed.*, 2000, **39**, 2263–2266.
27 D. Ghosh, M. Górecki, G. Pescitelli and K. K. Damodaran, *Angew. Chem., Int. Ed.*, 2021, **60**, 24406–24410.
28 R. Luboradzki, O. Gronwald, M. Ikeda, S. Shinkai and D. N. Reinhoudt, *Tetrahedron*, 2000, **56**, 9595–9599.
29 A. R. Hirst, D. K. Smith, M. C. Feiters, H. P. M. Geurts and A. C. Wright, *J. Am. Chem. Soc.*, 2003, **125**, 9010–9011.
30 S. L. James, G. O. Lloyd and J. Zhang, *CrystEngComm*, 2015, **17**, 7976–7977.
31 O. Lebel, M. Perron, T. Maris, S. F. Zalzal, A. Nanci and J. D. Wuest, *Chem. Mater.*, 2006, **18**, 3616–3626.
32 J. A. Foster, M. M. Piepenbrock, G. O. Lloyd, N. Clarke, J. A. K. Howard and J. W. Steed, *Nat. Chem.*, 2010, **2**, 1037–1043.
33 E. R. Draper and D. J. Adams, *Chem. Soc. Rev.*, 2018, **47**, 3395–3405.
34 D. Díaz Díaz, D. Kühbeck and R. J. Koopmans, *Chem. Soc. Rev.*, 2011, **40**, 427–448.
35 Z. Yang, G. Liang and B. Xu, *Acc. Chem. Res.*, 2008, **41**(2), 315–326.
36 X. Du, J. Zhou, J. Shi and B. Xu, *Chem. Rev.*, 2015, **115**(24), 13165–13307.
37 F. Zhao, M. L. Ma and B. Xu, *Chem. Soc. Rev.*, 2009, **38**, 883–891.
38 P. Dastidar, R. Roy, R. Parveen and K. Sarkar, *Adv. Ther.*, 2019, **2**, 1800061.
39 Q. Qian, D. Wang, L. Shi, Z. Zhang, J. Qian, J. Shen, C. Yu and X. Zhu, *Biomaterials*, 2021, **265**, 120403.
40 H. Zhang, S. Xu, J. Zhang, Z. Wang, D. Liu, L. Guo, C. Cheng, Y. Cheng, D. Xu, M. G. Kong, M. Rong and P. K. Chu, *Biomaterials*, 2021, **276**, 121057.
41 G. Gao, Y.-W. Jiang, W. Zhan, X. Liu, R. Tang, X. Sun, Y. Deng, L. Xu and G. Liang, *J. Am. Chem. Soc.*, 2022, **144**(26), 11897–11910.
42 P. Horcajada, C. Serre, M. Vallet-Regí, M. Sebban, F. Taulelle and G. Férey, *Angew. Chem., Int. Ed.*, 2006, **45**, 5974–5978.
43 E. Bellido, T. Hidalgo, M. V. Lozano, M. Guillevic, R. Simón-Vázquez, M. J. Santander-Ortega, Á. González-Fernández, C. Serre, M. J. Alonso and P. Horcajada, *Adv. Healthcare Mater.*, 2015, **4**, 1246–1257.
44 D. Cunha, M. Ben Yahia, S. Hall, S. R. Miller, H. Chevreau, E. Elkaïm, G. Maurin, P. Horcajada and C. Serre, *Chem. Mater.*, 2013, **25**, 2767–2776.
45 W.-H. Chen, X. Yu, W.-C. Liao, Y. S. Sohn, A. Cecconello, A. Kozell, R. Nechushtai and I. Willner, *Adv. Funct. Mater.*, 2017, **27**, 1702102.
46 Y. Wang, J. Yan, N. Wen, H. Xiong, S. Cai, Q. He, Y. Hu, D. Peng, Z. Liu and Y. Liu, *Biomaterials*, 2020, **230**, 119619.
47 P. Biswas and P. Dastidar, *Inorg. Chem.*, 2021, **60**(5), 3218–3231.
48 P. Biswas, H. K. Datta and P. Dastidar, *Chem. Commun.*, 2022, **58**, 969–972.
49 P. Biswas, H. K. Datta and P. Dastidar, *Biomater. Sci.*, 2022, **10**, 6201–6216.
50 C. P. Matos, Z. Adiguzel, Y. Yildizhan, B. Cevatemre, T. B. Onder, O. Cevik, P. Nunes, L. P. Ferreira, M. D. Carvalho, D. L. Campos, F. R. Pavan, J. C. Pessoa, M. H. Garcia, A. I. Tomaz, I. Correia and C. Acilan, *Eur. J. Med. Chem.*, 2019, **176**, 492–512.
51 M. Hussain, A. Javeed, M. Ashraf, N. Al-Zaubai, A. Stewart and M. M. Mukhtar, *Pharmacol. Res.*, 2012, **66**, 7–18.

52 C. Lang, C. Murgia, M. Leong, L.-W. Tan, G. Perozzi, D. Knight, R. Ruffin and P. Zalewski, *Am. J. Physiol.: Lung Cell. Mol. Physiol.*, 2007, **292**, L577–L584.
53 B. Xing, C.-W. Yu, K.-H. Chow, P.-L. Ho, D. Fu and B. Xu, *J. Am. Chem. Soc.*, 2002, **124**(50), 14846–14847.
54 L. A. Estroff and A. D. Hamilton, *Chem. Rev.*, 2004, **104**(3), 1201–1218.
55 M. George and R. G. Weiss, *Acc. Chem. Res.*, 2006, **39**(8), 489–497.
56 J. Hou, A. F. Sapnik and T. D. Bennett, *Chem. Sci.*, 2020, **11**, 310–323.
57 G. Cory, in *Scratch-wound assay: Methods in Molecular Biology Cell Migration Developmental Methods and Protocols*, ed. C. M. Wells and M. Parsons, Springer, London, 2011, pp. 25–30.
58 J. Deb, J. Majumder, S. Bhattacharyya and S. S. Jana, *BMC Cancer*, 2014, **14**, 567.
59 S. Toné, K. Sugimoto, K. Tanda, T. Suda, K. Uehira, H. Kanouchi, K. Samejima, Y. Minatogawa and W. C. Earnshaw, *Exp. Cell Res.*, 2007, **313**, 3635–3644.
60 D. Ngabire, Y. Seong, M. Patil, I. Niyonizigiye, Y. Seo and G. Kim, *Int. J. Oncol.*, 2018, **53**, 2300–2308.
61 B. Pucci, M. Kasten and A. Giordano, *Neoplasia*, 2000, **2**, 291–299.
62 Q. Liu, Z. Peng, L. Shen and L. Shen, *Front. Oncol.*, 2021, **11**, 737760.
63 C. W. Scharenberg, M. A. Harkey and B. Torok-Storb, *Blood*, 2002, **99**, 507–512.
64 A. Golebiewska, N. H. C. Brons, R. Bjerkvig and S. P. Niclou, *Cell Stem Cell*, 2011, **8**, 136–147.
65 V. Aggarwal, H. S. Tuli, A. Varol, F. Thakral, M. B. Yerer, K. Sak, M. Varol, A. Jain, M. A. Khan and G. Sethi, *Biomolecules*, 2019, **9**, 735.
66 R. Purpora, W. Massad, G. Ferrari, E. Reynoso, S. Criado, S. Miskoski, A. Pajares and N. A. García, *Photochem. Photobiol.*, 2013, **89**, 1463–1470.
67 S. S. Husain, I. L. Szabo and A. S. Tamawski, *Am. J. Gastroenterol.*, 2002, **97**, 542–553.
68 R. Kim, M. Emi, K. Tanabe and K. Arihiro, *Cancer Res.*, 2006, **66**, 5527.
69 D. G. DeNardo and L. M. Coussens, *Breast Cancer Res.*, 2007, **9**, 212.
70 T. Marsh, K. Pietras and S. S. McAllister, *Biochim. Biophys. Acta*, 2013, **1832**, 1070.
71 J. Liu, X. Geng, J. Hou and G. Wu, *Cancer Cell Int.*, 2021, **21**, 389.
72 B. Ruffell and L. M. Coussens, *Cancer Cell*, 2015, **27**, 462–472.
73 R. Afik, E. Zigmond, M. Vugman, M. Klepfish, E. Shimshoni, M. Pasmanik-Chor, A. Shenoy, E. Bassat, Z. Halpern, T. Geiger, I. Sagi and C. Varol, *J. Exp. Med.*, 2016, **213**, 2315–2331.
74 S. Tiainen, R. Tumelius, K. Rilla, K. Hämäläinen, M. Tammi, R. Tammi, V.-M. Kosma, S. Oikari and P. Auvinen, *Histopathology*, 2015, **66**, 873–883.
75 S. Srinivas and D. Feldman, *Anticancer Res.*, 2009, **29**, 3605–3610.
76 E. P. Chen and E. M. Smyth, *Prostaglandins Other Lipid Mediators*, 2011, **96**, 14–20.
77 A. V. Timoshenko, G. Xu, S. Chakrabarti, P. K. Lala and C. Chakraborty, *Exp. Cell Res.*, 2003, **289**, 265–274.
78 C. Y. Wu, K. Wang, J. F. McDyer and R. A. Seder, *J. Immunol.*, 1998, **161**, 2723–2730.
79 B. Burkholder, R.-Y. Huang, R. Burgess, S. Luo, V. S. Jones, W. Zhang, Z.-Q. Lv, C.-Y. Gao, B.-L. Wang, Y.-M. Zhang and R.-P. Huang, *Biochim. Biophys. Acta*, 2014, **1845**, 182–201.
80 D. Skrombolas and J. G. Frelinger, *Expert Rev. Clin. Immunol.*, 2014, **10**, 207–217.
81 S. A. Rosenberg, *J. Immunol.*, 2014, **192**, 5451–5458.
82 T. Jiang, C. Zhou and S. Ren, *OncoImmunology*, 2016, **5**, e1163462.